The International Journal of Advanced Manufacturing Technology (2023) 129:3353–3374
https://doi.org/10.1007/s00170-023-12346-5

ORIGINAL ARTICLE

An inverse method for automatic determination of material models for metal cutting based on multi-objective optimization

Hui Liu[1] · Anna Kibireva[1] · Markus Meurer[1] · Thomas Bergs[1,2]

Received: 26 May 2023 / Accepted: 17 September 2023 / Published online: 25 October 2023

Abstract

Cutting simulation is a crucial tool that enables engineers and operators to optimize machining processes virtually, before producing physical parts. The accuracy of these simulations relies heavily on validated models, encompassing both friction and material parameters. The prevalent technique for calibrating material models in cutting simulations is the inverse method. This state-of-the-art approach indirectly determines model parameters by comparing simulated outcomes with experimental data. However, the manual calibration process can be complex and time-consuming due to the intricacies of numerical simulation setups and the abundance of material model parameters. To address these challenges, this paper presents a novel fully-automated calibration approach utilizing multi-objective optimization algorithms. This approach integrates a modular design, simplifying the calibration process and enabling automatic calibration of any model parameters within cutting simulations. The approach has been successfully applied to calibrate the model parameters of AISI 1045 and X30CrMoN15-1 materials. Moreover, through a comparison of various optimization algorithms, this paper underscores the efficiency of the swarm optimizer in calibrating model parameters, particularly in scenarios with restricted computational resources.

Keywords Cutting simulation · Material model · Multi-objective optimization · Coupled Eulerian-Lagrangian · AISI 1045 · X30CrMoN15-1

Nomenclature

Symbol	Unit	Meaning
A	MPa	Yield stress at ε_0 and T_0
B	–	Factor of strain hardening
C	–	Factor of strain-rate hardening
C_1, C_2	–	Factor of particle velocity in the PSO algorithm
E	GPa	Young's modulus
F_n	N	Normal force
F_τ	N	Tangential force
F_y	N	Process force in y-direction
F_z	N	Process force in z-direction
F_c	N	Cutting force
h_c	$mW \cdot mm^{-2} \cdot K^{-1}$	Contact heat transfer coefficient
h_{ch}	mm	Chip thickness
h_e	mm	Uncut chip thickness
k	$kg/(s^3 \cdot K)$	Thermal contact conductance coefficient
l_{ch}	mm	Chip length
m and m_r	–	Index of temperature
n	–	Index of strain hardening
p	–	Position of a particle
R_a	μm	Arithmetic average roughness height
r_β	μm	Cutting edge radius
R_m	GPa	Yield strength
$R_{p0.2}$	GPa	Offset yield point
t	mm	Depth of engagement
T	$°C$	Temperature
T_0	$°C$	Room temperature
T_{melt}	$°C$	Melting temperature
T_f	$°C$	Reference temperature of friction
v_c	m/min	Cutting velocity

✉ Hui Liu
h.liu@wzl.rwth-aachen.de

[1] Laboratory for Machine Tools and Production Engineering (WZL) of RWTH Aachen University, Campus-Boulevard 30, 52074 Aachen, Germany

[2] Fraunhofer Institute for Production Technology IPT, Steinbachstr. 17, 52074 Aachen, Germany

v_i	–	Particle velocity in the PSO algorithm
v_r	m/min	Linear velocity
α	°	Tool rake angle
α_r	°	Friction angle
α_t	m^2/s	Thermal diffusivity
β	–	Factor of contact thermal conductivity
ε	–	Equivalent plastic strain
$\dot{\varepsilon}$	s^{-1}	Plastic strain rate
$\dot{\varepsilon}_0$	s^{-1}	Reference plastic strain rate
γ	°	Rake face angle
λ_{ch}	–	Chip compression ratio
μ	–	Friction coefficient
μ_0	–	Friction coefficient at ambient condition
ω_t	–	Index of contact heat transfer model
ω	–	Weighting factor of the particle velocity
ϕ	°	Shear angle

Abbreviations

Abb.	Description
API	Application Programming Interface
CBN	Cubic Boron Nitride
CEL	Coupled Eulerian-Lagrangian
EVF	Eulerian Volume Fraction
FEM	Finite Element Methode
GA	Genetic Algorithm
J-C	Johnson-Cook constitutive model
NSGA	Non-dominance Sorting Genetic Algorithm
PSO	Particle Swarm Optimization
SHPB	Split-Hopkinson Pressure Bar
SMPSO	Speed-constrained Multi-objective PSO

1 Introduction

Cutting is one of the most widely used technologies in the manufacturing industry. The global precision machining market is estimated to reach USD 11.8 billion by 2020 and is expected to grow at a compound annual growth rate of 6.6 % from 2021 to 2028 [1]. Market growth is driven by increasing demand for improved accuracy and production efficiency [1, 2]. To optimize the cutting processes, extensive experimental investigations have been carried out over the past decades. Unfortunately, the results obtained by experiments and the empirical models are are usually valid only for the cutting conditions used and are highly dependent on the accuracy of the experimental equipment [3]. A further disadvantage of the experimental approach is the high financial and time cost [4]. Therefore, researchers have been attempting for decades to create models to predict and optimize the cutting process.

Besides empirical models, there are two other approaches to modeling machining processes, namely analytical models and numerical models [5]. The review article by Arrazola et al. [6] summarizes recent advances in the field of analytical models and points out that while such models can predict important process state variables such as strain, stress, and temperature distribution, their over-simplification limits their ability to predict outcomes in complex processes and thus does not fully meet the requirements of industrial practice. Compared to analytical models, numerical simulations offer a more comprehensive understanding of the scientific nature of chip formation, enabling a more flexible application to different machining processes. Moreover, phenomena such as microstructure evolution, cracking, and roughness can be predicted by numerical simulation, which are crucial for parts with high safety requirements [7].

With the development of computer hardware and software, the ease of use and computational speed of numerical simulations have been significantly improved. However, the success and reliability of numerical cutting simulation depend on an accurate description of the elastic and viscoplastic properties of the workpiece material under cutting conditions as well as the friction between the tool and the workpiece [8]. For cutting simulations, the material model should include static behavior, yield stress behavior, dynamic recovery, and thermal softening due to recrystallization [6]. One of the most commonly used material models is the Johnson-Cook model. The model is applicable to material deformations in a wide range from $\dot{\varepsilon} = 10^3$ to $10^6\ s^{-1}$ and the effects of state parameters are considered separately, which facilitates the calibration of coefficients and has good numerical robustness [7]. In recent development, the Johnson-Cook model has been modified in various ways to more accurately describe dynamic deformation. Review papers [6–8] summarize several modified Johnson-Cook models suitable for different materials. Material models typically contain more than five calibration parameters. These parameters are usually identified iteratively by fitting measured yield curves by nonlinear regression or least squares. Mandatorily, the yield curves are derived from the loading conditions during the cutting process. This poses a serious challenge because dynamic materials testing equipment, such as Split-Hopkinson Pressure Bar (SHPB) [9] or Taylor's Impact tests, cannot account for the combination of high heating rates ($>1000\ °C/s$) and high loading rates (up to $\dot{\varepsilon} = 10^6\ s^{-1}$) that occur in the cutting process [10]. To obtain reliable model parameters, many researchers have been attempting to inverse calibrate the material model [6]. In the inverse approach, the verification process is simulated by interactively changing the material

model parameters to minimize the difference between the simulated and measured process state variables (e.g. chip shape, cutting forces, temperature, etc.) [11].

Özel and Altan pioneered the inverse methods for determining material models for cutting simulations [12]. They started the calibration with yield stress data at low strains and strain rates and extrapolated for high strain rates. After calibration, the deviation between the measured and simulated cutting and thrust forces was less than 10 %. The limitation of their approach is that they did not consider chip morphology (chip compression, chip curvature) in the validation and are limited to continuous chip formation. Shrot et al. [13] further developed the inverse method and considered chip curvature in the calibration. They introduced the Levenberg-Marquardt algorithm to optimize the parameters to significantly reduce the number of iterations. However, the optimization process was only applied to a single cutting condition and did not provide support for multiple conditions. Klocke et al. [14] considered both the maximum tool temperature and the serrated chip in their calibration. The chip thickness, serration height, and the serration frequency were used as calibration criteria. Bäker [15] used cutting forces and shear angles as validation parameters for the inverse calibration. The unique feature of his work is the use of a Python script to evaluate the shear angles and cutting forces of the simulation results, which partially automates the calibration.

Inverse calibration is a reliable approach for determining material models, but can be time-consuming due to lengthy numerical simulations, numerous calibration parameters, and multiple trial-and-error iterations. In addition, considering multiple cutting conditions simultaneously increases the number of simulations required, further increasing computation time. To increase efficiency, it is necessary to use optimization algorithms to minimize the number of iterations and expedite the determination of material parameters. To date, optimization algorithms have been widely used to determine the optimal parameters for machining processes. In particular, population-based metaheuristic optimization has significant advantages as, as it is able to efficiently determine the solution space while avoiding falling into local optima [16]. The review article by Yusup et al. [17] summarizes the application of optimization algorithms in cutting process and points out that both Genetic Algorithm (GA) and Particle Swarm Optimization (PSO) offer advantages in efficiency and accuracy compared to other population-based methods. Ozel and Karpat [18] applied the PSO algorithm to calibrate the parameters of the constitutive Johnson-Cook model. They used stress-strain relationships derived from SHPB and orthogonal cutting as calibration references. Their results demonstrate the efficiency of the PSO method in determining the parameters of the material model. Hardt et al. [19] combined a numerical orthogonal cutting simulation with the PSO algorithm to achieve calibration of a cutting condition within 40 iterations. The drawback of their work is that each iteration has to be started and evaluated manually, which requires a high personnel effort. The scientific results so far show that a fully automatic inverse calibration of material models with numerical simulation and optimization algorithms has not yet been achieved. This deficit was addressed in this paper.

The innovation in this work lies in the development of an automated procedure for the inverse calibration of material models. Instead of relying on labor-intensive and error-prone manual methods, this approach streamlines the calibration process, enabling faster and more accurate adjustments to material models based on experimental data. It efficiently explores a wide parameter space and ensures more accurate material models. Additionally, the procedure can adaptively recalibrate as new data becomes available. Automated calibration significantly reduces both time and cost, particularly beneficial in simulation-based process design. It also effectively manages complex models with numerous parameters and can integrate with other systems for advanced, real-time self-calibration.

The procedure consists of two steps. Firstly, numerical orthogonal cutting simulations are automatically generated, executed, and evaluated. Secondly, the cutting simulation is integrated with a multi-objective optimization algorithm through a software interface. The optimization algorithm generates parameters that are applied to the simulation, and the results are analyzed to provide feedback on the accuracy of the parameters. This process is repeated until the parameters are optimized to achieve automatic parameter determination. To validate the reliability of this procedure, material models of two workpiece materials were calibrated: carbon steel AISI 1045 and stainless steel X30CrMoN15-1. Moreover, the experimental method for determining the reference data, such as cutting forces and friction coefficient, is described. The simulation and the experimental method together provide a comprehensive scheme for material model calibration.

The following section first describes the experimental setup used to determine the calibration reference. In Section 3, numerical cutting simulations are presented based on the coupled Eulerian-Lagrangian (CEL) method, and the automation of the simulation process is explained. Section 4 details two optimization algorithms used to determine the model parameters, while Section 5 presents the efficiency, accuracy, and calibration results of these algorithms. Additionally, Section 5 also discusses the effect of cutting conditions on chip thickness, introducing the Péclet number. Finally, the last section summarizes the proposed method's advantages and shortcomings and provides suggestions for future development.

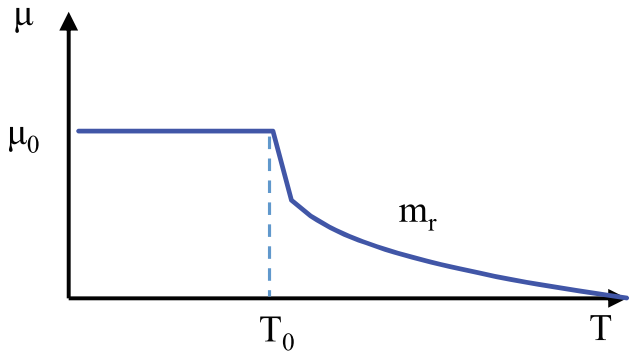

Fig. 1 Temperature dependence of friction coefficient based on Puls model [21]

2 Experimental setup for model validation

Reliable experimental data are the basis for successful model calibration. This section presents the experimental setup for determining the coefficient of friction and performing orthogonal cutting. The characteristics of the two workpiece materials as well as the cutting tools are also outlined.

2.1 Experimental setup for determination of the friction coefficient

The tribological performance during the cutting process is a critical aspect in machining procedures that affects contact behavior and leads to temperature rise [20]. To accurately replicate the material behavior in metal cutting, it is essential to establish the frictional characteristics between the tool and workpiece material. Hence, in this study, a temperature-dependent friction model developed by Puls et al. [21] has been implemented and is presented in Eq. 1:

$$\mu = \mu_0 \cdot \left[1 - \left(\frac{T - T_0}{T_{melt} - T_0}\right)^{m_r}\right] \tag{1}$$

The model postulates that the apparent friction coefficient, μ, remains constant at temperatures below the critical threshold temperature, T_0. However, as the temperature in the cutting zone surpasses T_0, μ exhibits a decreasing trend with increasing temperature within the cutting zone. The visual representation of this model is shown in Fig. 1.

To investigate the tribological properties of the systems, friction experiments were conducted. These experiments aimed to identify the friction model parameters and the apparent coefficient of friction under high strain rates and temperatures in the tool-workpiece contact zone. The experiments were performed using the FORST RASX 8 × 2200 × 600 M/CNC vertical broaching machine, as shown in Fig. 2a. The workpieces (Fig. 2b,2), were attached to the vertical machine slide to enable metal forming. In contrast to the traditional broaching method, the workpiece was clamped within a specialized fixture located in the tool holder, which typically houses the broaching tool clamping mechanism. All samples were moved longitudinally against the tool, creating sliding contact between the flank face and the workpiece material. To enable metal forming process, prevent cutting and supress the chip formation, indexable C-type inserts were flipped over, creating large negative rake angle and reducing the clearance angle. The inserts were inclined at an angle of α_r = 10° and fixed in a custom-built tool holder (Fig. 2b,5). The measuring of the resulting force components acting on the system was performed using the 3-component piezoelectric dynamometer KISTLER Z21289

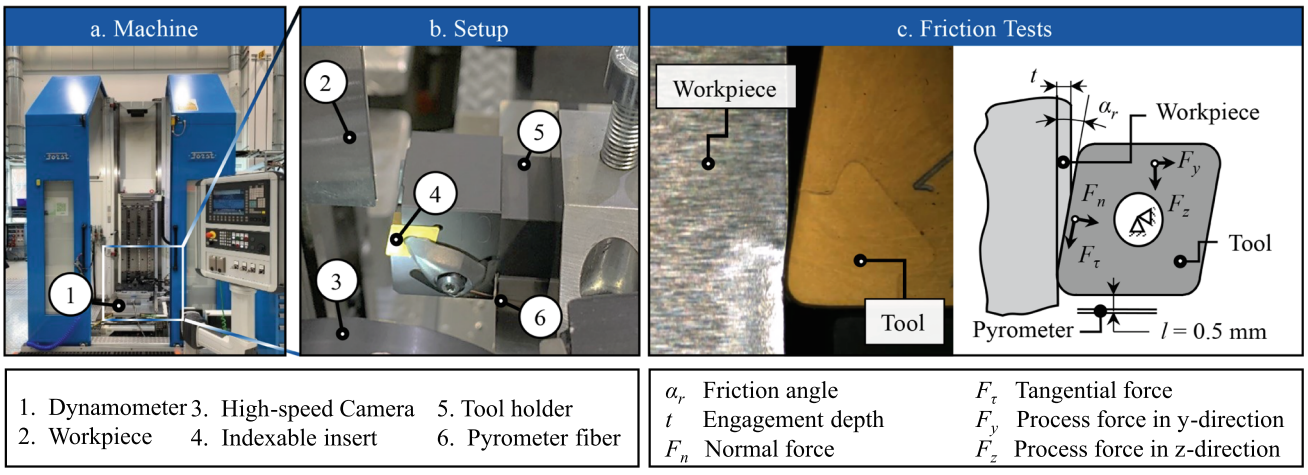

Fig. 2 Experimental setup for determination of the friction coefficient

Table 1 Friction tests parameters

Workpiece material	Tool material	Linear velocity v_r $[m/min]$	Depth of engagement t $[mm]$	Friction angle α_r [°]
X30CrMoN15-1	CBN	50, 75, 100, 125, 150	0.2	10
AISI 1045	WC-6Co	20, 40, 60, 80, 100	0.5, 1	10

(Fig. 2a,1) with a measuring range ±80kN. The recording of the test was performed with a high-speed camera Phantom v7.3 (Fig. 2b,3) with recording rate of 6698 Hz at a 800 × 600 - resolution. The high-speed camera ensured the geometrical position of the inserts. Additionally, to measure the workpiece temperature, a two-color pyrometer fiber (Fig. 2b,6) was placed behind the friction zone at a distance of $l = 0.5\ mm$, as shown in Fig. 2c.

The relative friction coefficients were calculated by dividing tangential forces F_τ by normal forces F_n, as defined in Eq. 2 [5].

$$\mu = \frac{F_\tau}{F_n} = \frac{F_z \cdot \cos\alpha_r - F_y \cdot \sin\alpha_r}{F_y \cdot \cos\alpha_r + F_z \cdot \sin\alpha_r} \tag{2}$$

Table 1 lists the selected linear velocities v_r, which are based on the corresponding cutting speeds for the subsequent cutting process. To prevent tool failure from impact loading and to ensure sufficient contact between the CBN tool tip and the workpiece material, the depth of engagement for CBN is set at $t = 0.2\ mm$. For the carbide WC-6Co, which has better ductility than the CBN material, a depth of engagement of t = 0.5 and 1 mm is selected, taking into consideration its material properties. The measured process forces in x and y-direction as well as the workpiece temperature are shown in Fig. 3.

To calibrate and validate the friction model (Eq. 1) three parameters - μ_0, T_0, and m_r - need to be determined. One approach for determining these at higher strain rates is inverse identification. This involves conducting a series of finite element method (FEM) simulations using different model parameters, obtained with curve fitting and comparing the resulting modeling data to experimental values. The simulation parameters were iteratively adjusted until the modeled results (cutting forces and temperatures) match the experimental values. The parameters of the temperature-dependent friction model have been determined and are presented in Table 2.

2.2 Experimental setup of orthogonal cutting

Following the the friction experiments, orthogonal cutting tests were conducted on the FORST RASX 8×2200×600 M/CNC vertical broaching machine. Likewise the friction experiments, the workpieces were to the broaching slide and moved vertically against a grooving tool, as shown in Fig. 4b. All cutting tests were performed without cutting fluid supply.

The cutting force components were measured using the dynamometer, while the high-speed camera recorded the chip formation process. Orthogonal cutting experiments were conducted with varying cutting speed (v_c) and uncut chip thickness (h_e), as outlined in Table 3. To enhance the sta-

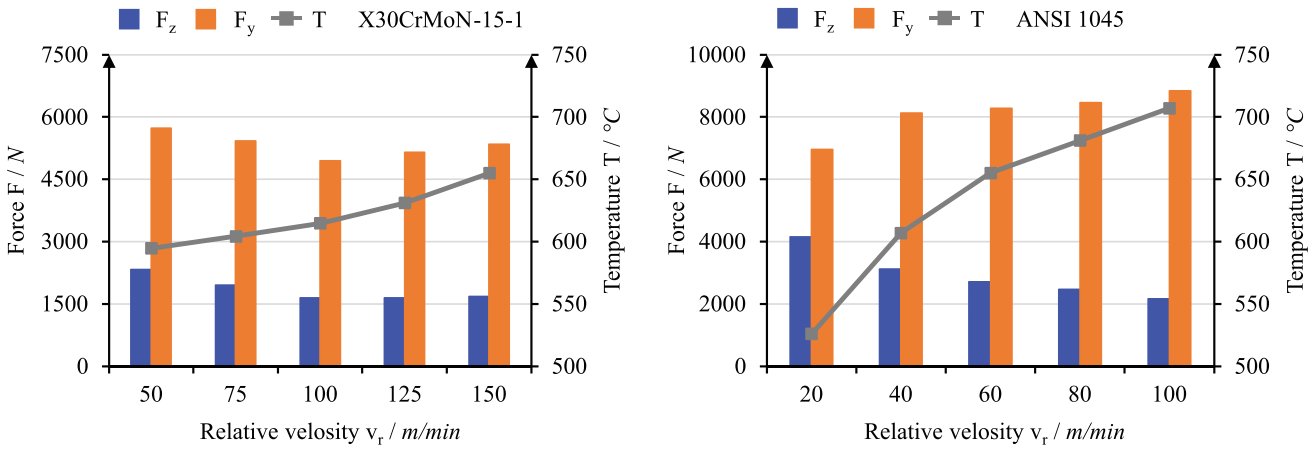

Fig. 3 Experimental results for friction tests [21, 22]

Table 2 Calibrated friction model parameters [21, 22]

Workpiece Material	Tool Material	μ_0 [-]	$T_{0,r}$ [$^\circ C$]	m_r [-]
X30CrMoN15-1	CBN	0.35	550	0.3
AISI 1045	Carbide WC-6Co	0.7	600	0.35

tistical reliability, the orthogonal cutting tests were repeated twice.

After cutting, the chip thickness was measured to calibrate the material model in the cutting simulation. Fig. 5 shows the chip embedded in epoxy resin on the left side. Under the microscope, the chip edge is visible, allowing precise thickness measurements. On the right side of Fig. 5, slight differences in thickness can be seen between the different positions.

2.3 Properties of the workpieces and the cutting tools

In the present study, two workpiece materials were investigated, namely the medium-carbon steel AISI 1045 and the martensitic grade X30CrMoN-15-1 in annealed condition. The workpieces were shaped in the form of rectangular plates with dimensions of $50 \times 40 \times 3\,mm$. The microstructure and chemical composition of these materials were analyzed using spark spectroscopy, and the results are presented in Fig. 6.

Both AISI 1045 and X30CrMoN-15-1 materials exhibit a homogeneous microstructure. X30CrMoN-15-1 has a finer ferrite phase and undissolved precipitates, which lead to higher strength compared to AISI 1045.

The CBN CNGA120408 and H13A CNGA120408 inserts from Sandvik were used for the friction tests. The arithmetic mean roughness (Ra) of the flanks was measured to be 0.46 μm and 0.33 μm for the two types of tools respectively. Two types of tailor-made grooving plates were used for orthogonal cutting, and their geometrical properties are summarized in Table 4. The geometry was defined in collaboration with industry users to ensure good transferability of the results.

3 Coupled Eulerian-Lagrangian (CEL) method for the simulation of cutting processes

Cutting simulation is one of the most challenging topics in process simulation, as conventional numerical methods based on the Lagrangian approach have difficulties in simulating large deformations in the cutting process due to mesh distortions. In this paper, the Abaqus/Explicit coupled Euler-Lagrange (CEL) method is used to address these large strain rates during cutting. The CEL method is widely used in various machining simulations, including milling [23, 24] and turning [19], due to its unique stability and good computational efficiency. The following subsections explain the CEL-based cutting simulation in terms of the model setup. The mathematical principles for computing the model can be found in paper [25].

3.1 Model setup of the chip formation simulation

Utilizing the CEL method, the cutting tool, which doesn't undergo significant deformation, is discretized using Lagrangian elements. Workpieces displaying considerable deformations, on the other hand, are represented using Eulerian elements. The model setup for orthogonal cutting and the

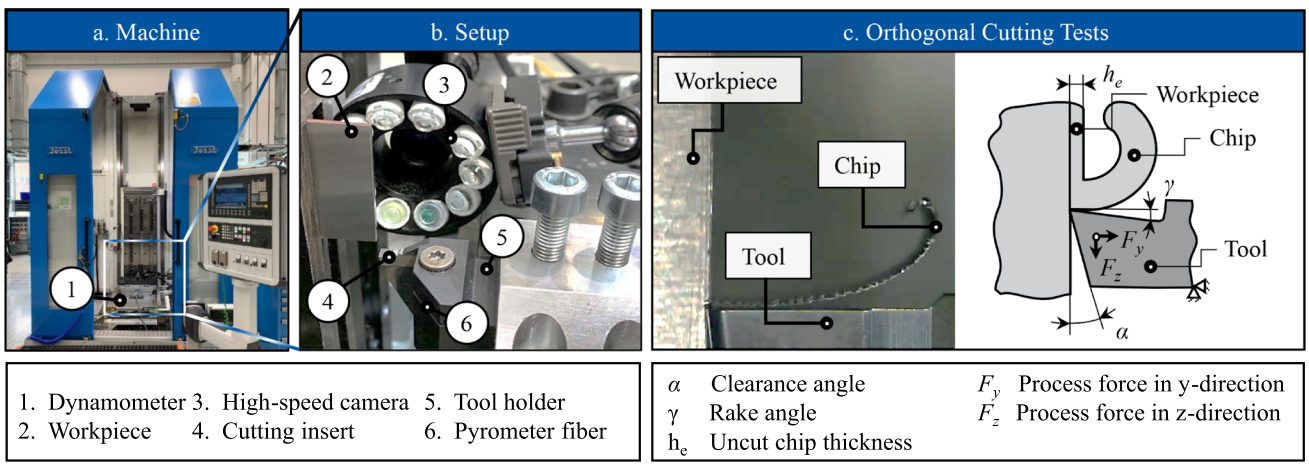

Fig. 4 Experimental setup for determination of the friction coefficient

Table 3 Orthogonal cutting test parameters

Workpiece material	Tool material	Cutting velocity v_c $[m/min]$	Uncut chip thickness h_e $[\mu m]$
X30CrMoN15-1	CBN	110, 130	30, 50, 70
X30CrMoN15-1	CBN	100, 125, 150	20, 40, 60, 80
AISI 1045	Carbide WC-6Co	60, 80, 100, 120, 150	100, 200, 300

associated boundary conditions are illustrated in Fig. 7. The grid-independence validation method ascertained the appropriate grid size for accurately capturing the temperature and stress gradients within the cutting area. The workpiece grid was set at 6 microns, and the tool's mesh size was specified as 6 microns at the tip, extending to 100 microns in areas beyond the tip. The tool is considered as an ideal rigid body, and therefore, the simulation ignores the wear and deformation of the tool. The upper and rear surfaces of the tool outside the cutting area are set as isothermal boundaries with a constant temperature of $T_{room} = 25\,^{\circ}C$. The contact thermal conductivity h_c between the tool and the workpiece is defined by a pressure-dependent model, as shown in Eq. 3 to accurately account for thermal effects.

$$h_c = \omega_c \cdot \beta \cdot p^{0.985} \tag{3}$$

where β is the temperature-dependent material coefficient described in [24]. The model parameter ω_c equals 1.6 for AISI 1045. In the simulation of X30CrMoN15-1, the small uncut chip thickness h_e results in high contact pressure, and therefore h_c is assumed to be the ideal thermal contact condition. The friction behavior between the tool and workpiece is described using the Puls friction model [21], which is explained in detail in Section 2.2.

Constitutive models are of central importance for the simulation of the flow stress behavior of workpiece materials at high strain rates and high temperatures in machining processes. A comprehensive review [8] discusses the most commonly used constitutive models for machining simulations. In particular, the Johnson-Cook (J-C) model [26] is the most popular model due to its simplicity and relatively straightforward calibration process. This standard J-C model can be implemented directly into most simulation software, including ABAQUS and Deform, without the need for additional programming. Consequently, it is easily transferable for different applications. This paper uses the J-C model as the material model for cutting simulation. Extensive experimental and simulation data are available for the model parameters of AISI 1045 steel. An overview of the different model parameters can be found in Table 5.

The calibration range of parameters for AISI 1045 was determined based on existing models, while for X30CrMoN15-1, the parameter range was estimated based on its mechanical properties, since no validated model was available as a reference. Table 6 shows the range settings for the subsequent automatic calibration process.

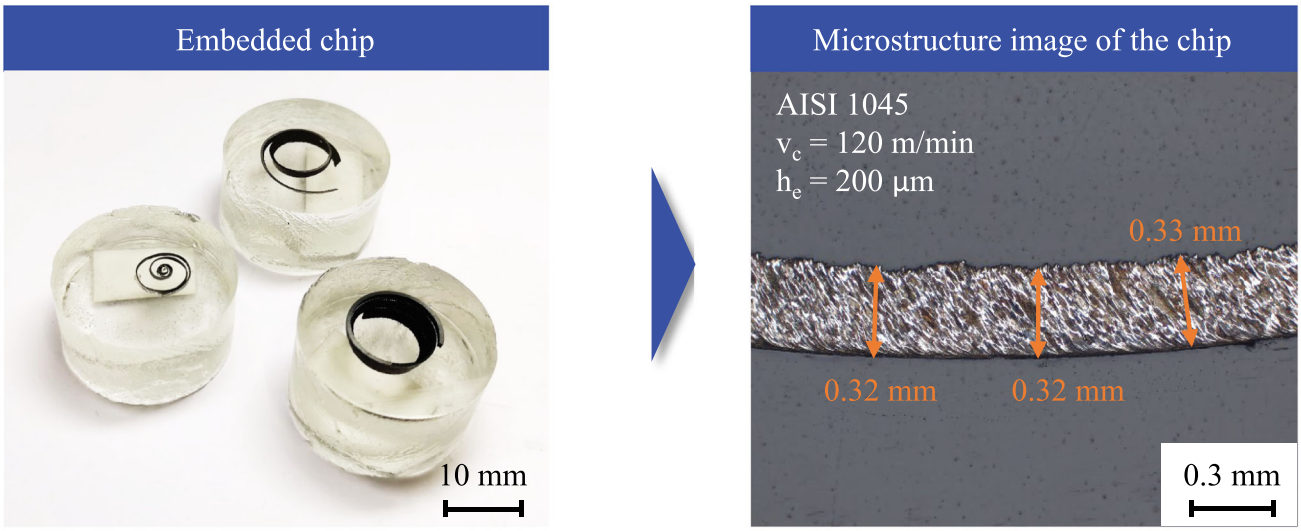

Fig. 5 Determination of chip thickness by microstructure image

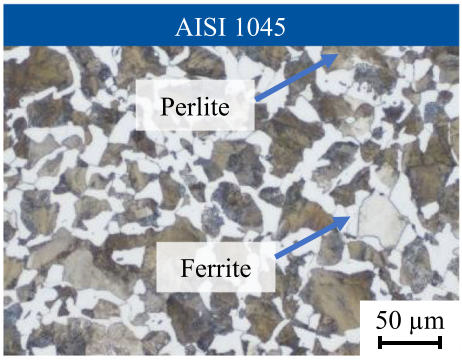

Element	C	Si	Mn	P	S
wt / %	0.469	0.145	0.686	0.0247	0.0261
Element	Cr	Ni	Cu	Mo	Al
wt / %	0.337	0.0866	0.0555	0.0356	0.0288
Physical properties	E	R_m	$R_{p0.2}$	k	Hardness
	GPa	MPa	MPa	W/m·k	HB
AISI 1045	210	695	392	51.9	200

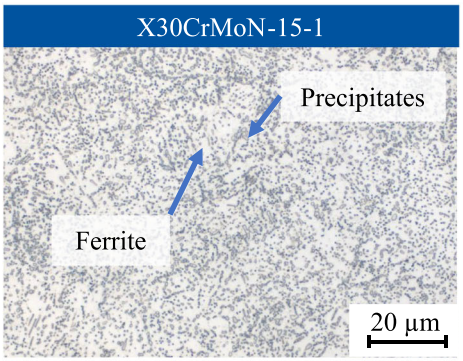

Element	C	Si	Mn	P	S
wt / %	0,291	0,572	0,452	0,031	0,0119
Element	Cr	Mo	Ni	Cu	N
wt / %	15,62	0,965	0.232	0.095	0.427
Physical properties	E	R_m	$R_{p0.2}$	k	Hardness
	GPa	MPa	MPa	W/m·k	HV
X30CrMoN-15-1	223	920	691	21,1	271

Fig. 6 Microstructure, mechanical properties and chemical composition of the workpiece materials

This study employs evaluation algorithms to determine the appropriate model parameters within a given range. The criteria include a comparison of simulated and experimental cutting force F_c and an evaluation of chip thickness. The cutting force F_c, aligned with the direction of the cutting speed v_c, determines the cutting power and heat generation during machining and serves as a calibration reference. In the following subsection, the method for deriving the chip thickness from the simulation results is explained in more detail.

3.2 Method for automatic execution and evaluation of chip formation simulations

In CEL simulations, the Euler volume fraction (EVF) indicates the presence or absence of a substance. The value of EVF is 1 for the region with matter and 0 for the region without matter. To evaluate the chip, a rectangular area above the cutting area (refer to Fig. 8) is chosen as the evaluation area, and grid nodes with EVF values between 0 and 1 are extracted to obtain the chip's outer contour. Typically, the chip's backside has a smooth curve, while the front side can be serrated or smooth, depending on the chip's morphology. To determine the nodes on the backside, the evaluation program traverses the contour points of the evaluation area from right to left, generating asymptotes (contour lines). Perpendicular lines are drawn on the contour lines at $10\mu m$ intervals to intersect the nodes on the front side of the chip. The chip thickness is calculated as the distance from the intersection point to the perpendicular base, as shown in Step 2 of Fig. 8. The study uses the average chip thickness as a criterion, but the method can also evaluate serrated chips by analyzing the frequency of height fluctuations.

In addition to the contour method, this study also uses the classical theory of shear plane to calculate the chip thickness. The position of the shear plane is determined by identifying the maximum shear stress in the cutting area. The chip thickness can be derived from the shear angle using the equation

Table 4 Geometric properties of grooving inserts for orthogonal cutting

Tool material	Rake angle γ [°]	Clearance angle α [°]	Cutting edge radius r_β [μm]
CBN	0	7	21.8 ± 6.3
Carbide WC-6Co H13A	12	3	5 ± 0.2

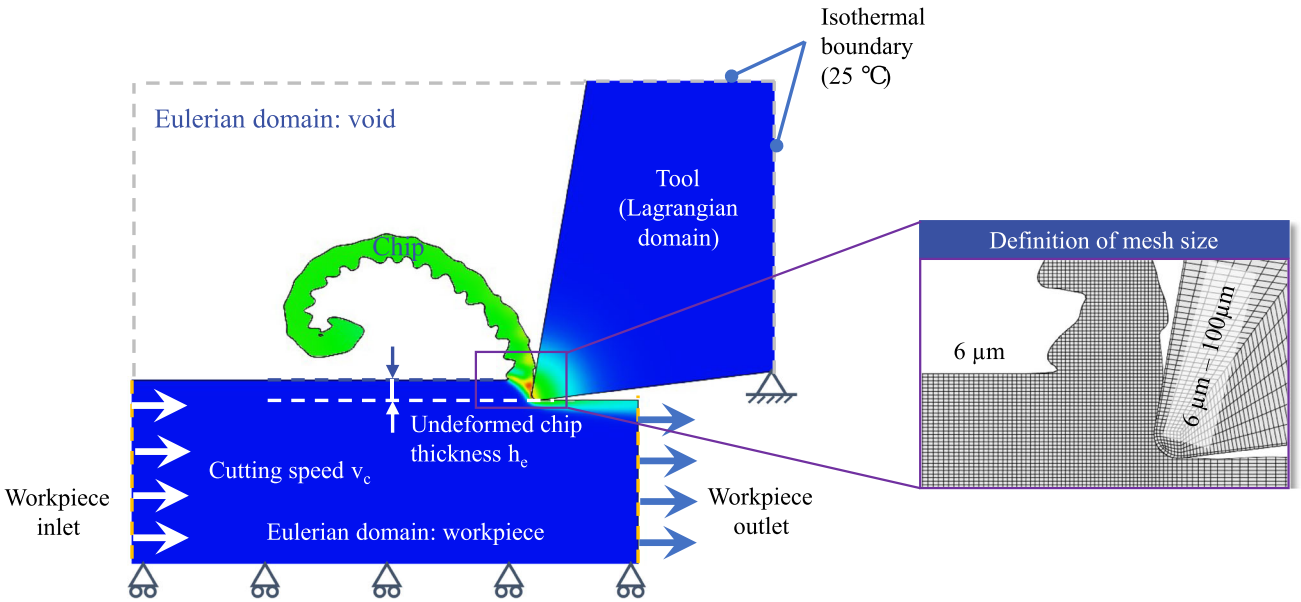

Fig. 7 Model setup of 2D-orthogonal cutting with the CEL-method

in step 4 of Fig. 8. Although the shear angle method is less accurate than the contour method, it is still useful as an alternative solution to validate the results of the contour method. In the later calibration process, chip thickness evaluations are performed for both methods, and if the difference between the two results is less than 10 %, the result of the contour method is used. Otherwise, the result is considered invalid.

4 Multi-objective optimization

The previous section described the procedure for automatically performing and evaluating numerical section simulations. In this section, the two population-based metaheuristic optimization algorithms used in this work are presented. Population-based metaheuristic algorithms are a class of approaches that search for near-optimal solutions by maintaining a set of proposed solutions and using the properties of the population to iteratively guide the search [33]. In recent years, such approaches have gained prominence in solving large global optimization problems due to their unique ability to handle multimodal landscapes, parallel computation, and general search capabilities [34]. Common algorithms in this category include: genetic algorithms, particle swarm optimization, ant colony optimization, wash frog jump
algorithms, and simulated annealing algorithms [33]. In selecting the algorithm, the following aspects are considered.

1. The algorithm should have good multiobjective optimization capability to consider the compatibility of material models under different cutting conditions.
2. The algorithm has been widely established and approved in the manufacturing industry and in research.
3. The algorithm has an open source run-time library based on the Python language, which ensures the reproducibility and simplicity of the methods presented in this paper.

According to the above aspects, the genetic algorithm NSGA-II and the particle swarm optimizer SMPSO are

Table 5 Johnson Cook material model of AISI 1045 according to the state of the art

	A [MPa]	B [MPa]	C –	m –	n –	T_m [°C]	T_0 [°C]	$\dot{\varepsilon}_0$ s^{-1}
Jaspers and Dautzenberg [27]	553.1	600.8	0.0134	1	0.234	1460	20	10^{-3}
Ee et al. [28]	310	815	0.05	2.624	0.22	1460	25	1
Zouhar and Piska [29]	375	552	0.02	1.4	0.457	1460	25	1
Saez-de-Buruaga et al. [30]	546	452.2	0.0308	0.6146	0.3514	1460	25	1
Treppmann [31]	250	250	0.15	1.2	0.24	1460	25	1
Klocke et al. [32]	546	487	0.027	0.631	0.25	1460	25	1

Table 6 Parameter range for the automatic calibration of the J-C model

Workpiece Material	*A* [MPa]	*B* [MPa]	*C* –	*m* –	*n* –
AISI 1045	250 - 600	250 - 900	0.0001 - 0.2	0.6 - 1.4	0.05 - 0.5
X30CrMoN15-1	400 - 800	300 - 800	0.0001 - 0.8	0.6 - 1.4	0.01 - 0.5

selected in this paper. Both algorithms have multi-objective formulation, which means that the optimization considers two or more cutting constraints simultaneously. Although other methods of multi-objective optimization exist, this paper does not delve into their theoretical formulation. Instead, the objective is to provide insight into automated parameter calibration by discussing the advantages and disadvantages of the two approaches. To apply the optimization algorithms in the cutting simulation, a Python-based open-source framework, jMetalPy, was used in this work. The software framework provides examples of ready-to-use processes as well as functional APIs that allow direct integration of the optimization algorithm into numerical simulations. The following subsections briefly describe the principles of the two algorithms as well as the multi-objective optimization. Subsequently, the procedure for combining optimization algorithms with the cutting simulation is explained in detail.

4.1 Genetic algorithm - NSGA-II

In nature, adaptability to the environment is critical for an individual's survival. This adaptability is controlled by genes, and only the fittest individuals survive and pass on their genes through a recombination process called crossover [35]. The Genetic Algorithm (GA) is based on the principle of survival of the fittest, as shown in Fig. 9, where the fittest individuals are selected for reproduction to create the next generation

In GA-based calibration of material models, each J-C parameter is considered as a gene. A set of material model

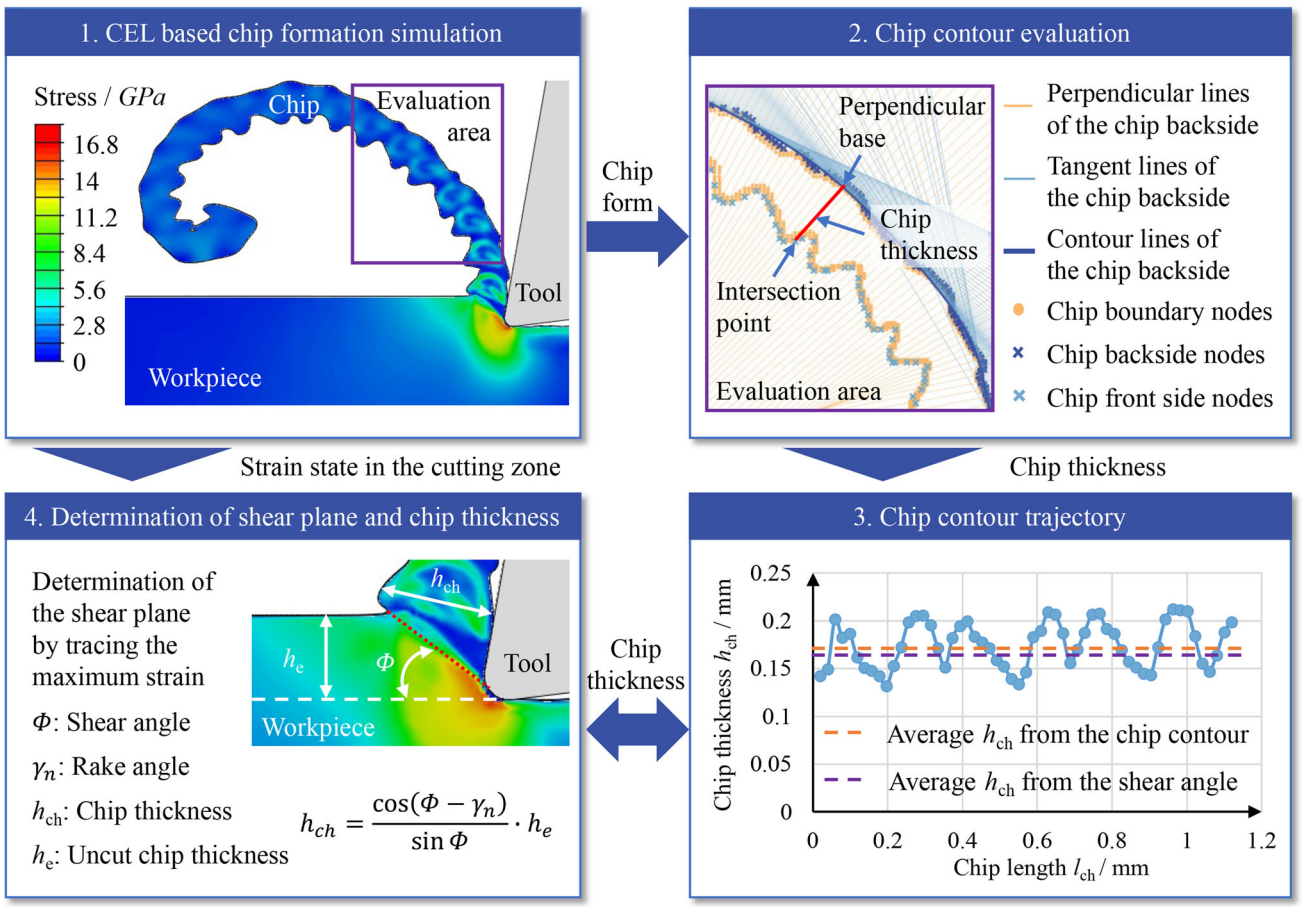

Fig. 8 Methods for the automatic evaluation of chip thickness during orthogonal cutting

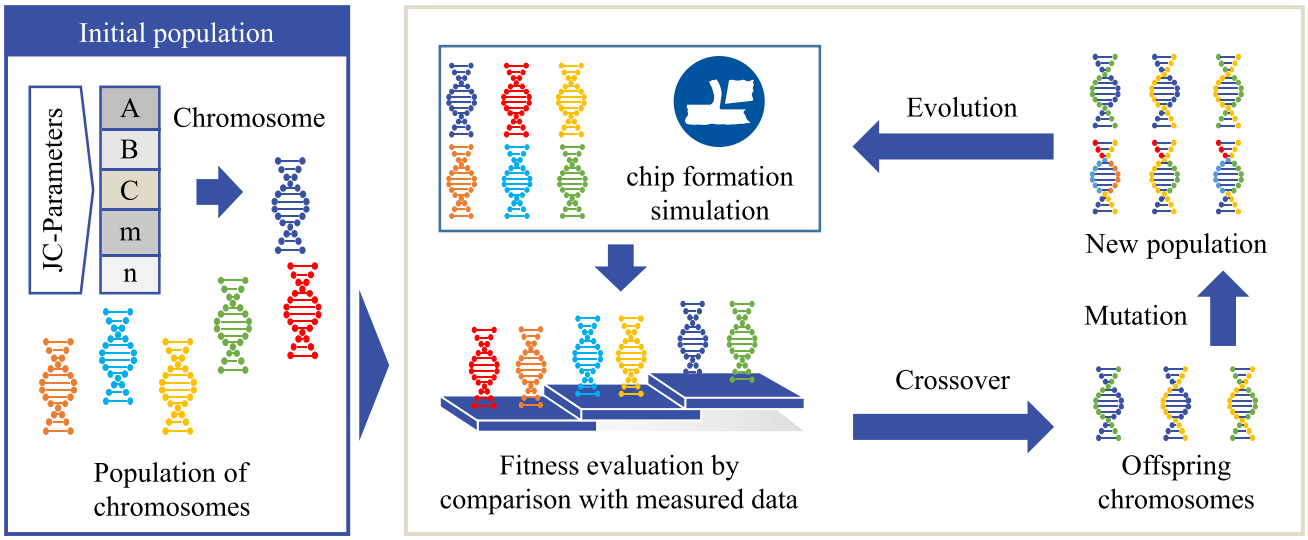

Fig. 9 Principle of NSGA-II optimization of J-C material parameters

parameters is combined to form a chromosome. The initial chromosome is randomly generated. In each iteration, the model parameters contained in the chromosome are first evaluated by applying them to a cutting simulation. The smaller the deviation of the simulation results from the experiment, the better the fitness of the chromosome. In the crossover step, the chromosomes with higher fitness are combined. To avoid sampling singularity and find the optimal solution in the global solution space, the chromosomes of the offspring are partially mutated randomly. The evolution process continues until a certain number of iterations is reached or the fitness of the chromosomes achieves a target value.

In a multi-objective calibration problem, the material model must satisfy multiple cutting conditions simultaneously. This can make it challenging to evaluate the fitness of different parameter combinations since some may be optimal for certain cutting conditions but suboptimal for others. To address this issue, the Non-Dominance Sorting Genetic Algorithm II (NSGA-II) uses non-dominance sorting and diversity-preserving mechanisms to select optimal solutions [36]. For instance, when considering a material model, two different parameter combinations A and B are compared. If A performs better than B under all cutting conditions, A dominates B, and otherwise, A and B are non-dominated. In NSGA-II, chromosomes that are non-dominated by any other chromosome form the non-dominated boundary (Pareto optimal solution). Chromosomes in the Pareto optimal solution are selected for crossover, while the algorithm considers chromosome differentiation (crowding-distance) in its selection. For further details on programming the NSGA-II algorithm, refer to Article [36].

4.2 Particle Swarm Optimizer - SMPSO

The particle swarm algorithm (PSO) was first proposed in 1995 by Kennedy et al. [37]. It is a bioinspired metaheuristic algorithm that mimics the social behavior of a flock of birds and is popular for solving optimization problems. The speed-constrained multi-objective PSO (SMPSO for short) is an improved multi-objective PSO that incorporates a velocity constriction procedure developed by Nebro et al. [38]. The operating principle of the SMPSO can be simplified in Fig. 10.

In the SMPSO algorithm, particles represent combinations of material model parameters, while the population of solutions is called a swarm. Initially, the particles are uniformly distributed across the entire solution space. The material model parameters contained in each particle are used in the cutting simulation to calculate the cutting state parameters. The quality of a solution represented by the particles is evaluated based on the difference between the simulated and experimental state parameters. After each evaluation, the particles move towards the optimal solution by adjusting the material parameters. The direction of motion is multi-dimensional, with the number of dimensions corresponding to the number of individual variables of the particle. For the J-C material model, each particle has five dimensions corresponding to the five material model parameters (A, B, C, m, and n). The position of a particle $\vec{p}_i\,(t)$ in iteration t can be formulated as follows:

$$\vec{p}_i\,(t) = \vec{p}_i\,(t-1) + \vec{v}_i\,(t) \tag{4}$$

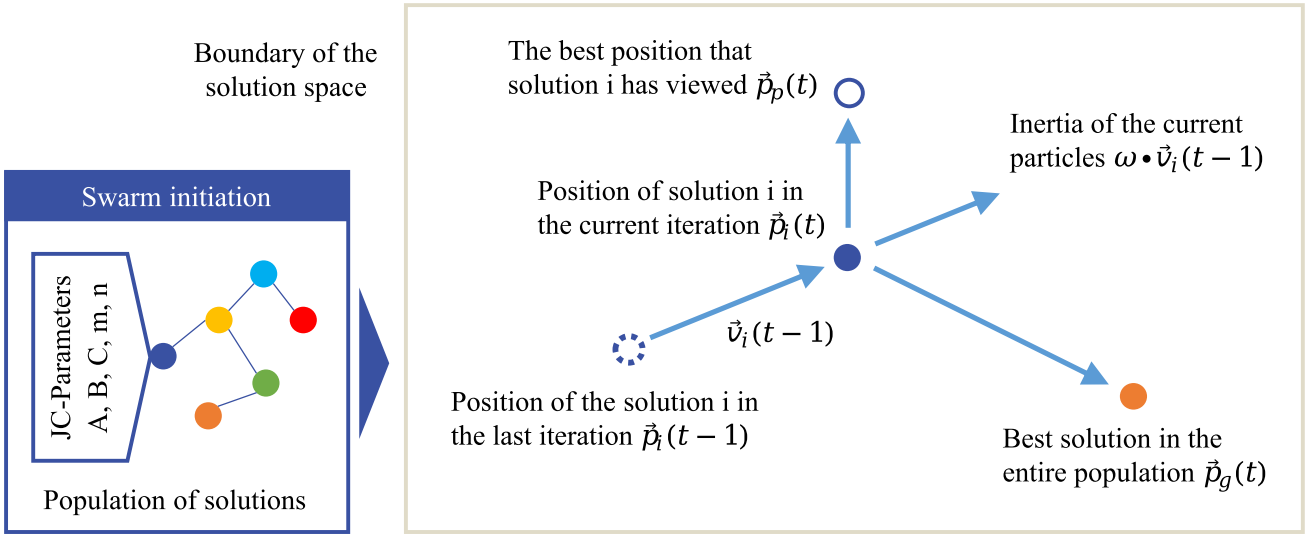

Fig. 10 Principle of SMPSO optimization of J-C material parameters

where the velocity vector $\vec{v}_i\ (t)$ is given by

$$\vec{v}_i\ (t) = \omega \cdot \vec{v}_i\ (t-1) + C_1 \cdot r_1 \cdot \left(\vec{p}_p - \vec{p}_i\right) + C_2 \cdot r_2 \cdot \left(\vec{p}_g - \vec{p}_i\right) \quad (5)$$

The direction of the velocity is affected by three constraints: the inertia of the particle $\vec{v}_i$, its individual historical best $\vec{p}_p$, and the global best $\vec{p}_g$. In a multi-objective optimization problem, there may be multiple optimal solutions, and $\vec{p}_g$ is then randomly selected from the set of Pareto-optimal solutions. The parameters C_1 and C_2 are random numbers between 1.5 and 2.5, while r_1 and r_2 are random numbers between 0 and 1 to reflect the subjective randomness of particle movement. To accelerate the convergence and prevent the particles from falling into the local optimum solution, the SMPSO algorithm also introduces the constriction coefficient to control the velocity magnitude and the mutation factor to control the velocity direction. A detailed description can be found in [38].

4.3 Procedure for the automatic calibration of material models

The jMetal framework is used for multiobjective optimization to automatically calibrate material models. The framework generates initial material model parameters within the range of parameters specified in Table 2. A Python subroutine replaces the initial parameters with the material model parameters of the pre-defined cutting simulation file[1]. The "subprocess" command can then be used to initiate the numerical cutting simulation. The "subprocess" command returns information about the success of the simulation. If the simulation runs successfully, the evaluation procedure described in Section 3.2 is executed. The fitness values of the simulation results are calculated by comparing the simulated and experimental cutting forces and chip thickness using the following equation:

$$\frac{1}{Fitness} = Deviation = \frac{|F_{c\_exp} - F_{c\_sim}|}{F_{c\_exp}} \cdot 0.7 + \frac{|h_{ch\_exp} - h_{ch\_sim}|}{h_{ch\_exp}} \cdot 0.3 \quad (6)$$

The larger the fitness value is, the better the simulation results match with the experiment. After completing the simulation, the fitness values are sent back to jMetal to generate new model parameters. This entire process, including parameter generation, simulation, and evaluation, is referred to as one iteration.

The jMetal framework settings are shown in Fig. 11. A population/swarm size of 6 is chosen for this study. Although larger populations can accelerate the search for optimal parameter values, they also result in an exponential increase in simulation time. For each iteration, 90 orthogonal cutting simulations are conducted for AISI 1045

[1] The cutting simulation file means the inp. file, which contains a complete description of the numerical model. The input file has a text format with keywords, so it can be easily modified by Python code.

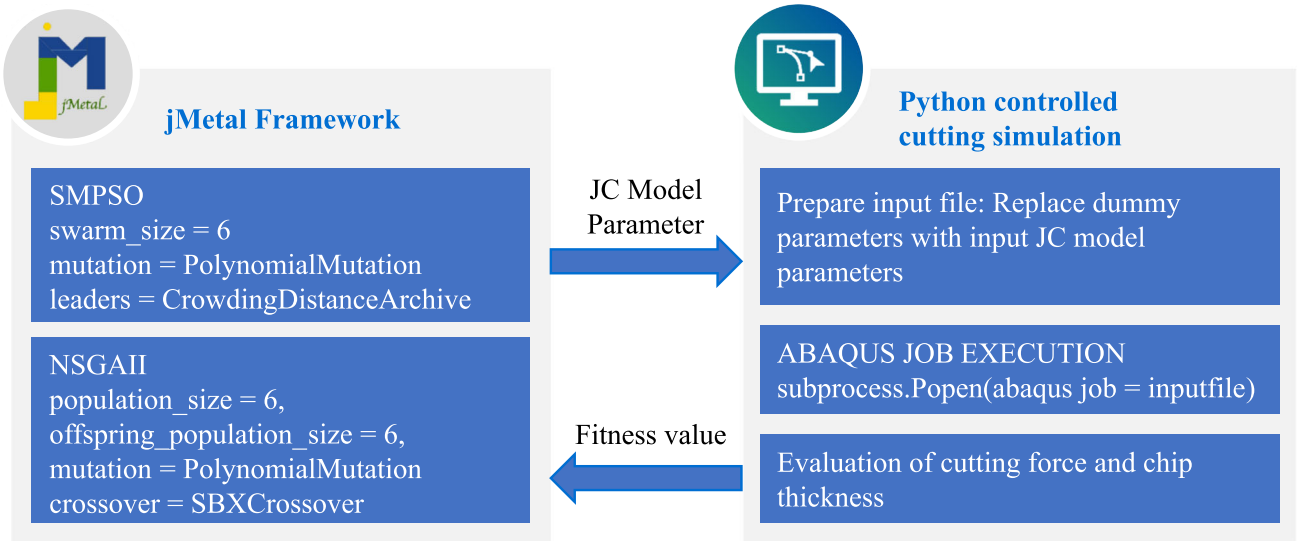

Fig. 11 Procedure of automatic material model calibration with jMetal framework

(15 cutting conditions × 6 population), and 108 simulations for X30CrMoN15-1. To expedite the simulation process, a high-performance computer[2] is used to run 15 simulations simultaneously, reducing the iteration time to 18 hours.

5 Results and discussion

This section presents the results of automatic calibration of material models by applying two different algorithms, the genetic algorithm NSGA-II and the particle swarm algorithm SMPSO. A comparison is made between the efficiency of these two methods in finding optimal material model parameters. In addition, the relationship between the AISI 1045 chip thickness and the cutting parameters is investigated.

5.1 Results of AISI 1045

The material model parameters are first calibrated using the NSGA-II genetic algorithm, and their fitness values over iterations are plotted in Fig. 12. The color scale in the plot indicates the level of agreement between simulation and experimental results. Darker colors signify higher levels of conformity.

At the outset, the generated parameters demonstrated significant deviation, with only one sample exhibiting deviation values of less than 30 % for specific cutting conditions. Nonetheless, as the iterations proceeded, all samples showed a decrease in deviation values, with simulation results continually optimized to match the experimental results. By the 23rd iteration, the simulation results indicated deviation values of less than 10 % from the experiment for h_e = 300 μm. However, for h_e = 100 and 200 μm, deviation values were generally higher than 10 %. The optimization process was focused excessively on the local optimization of large uncut chip thickness, while neglecting small uncut chip thickness. To overcome this issue, a larger population size was necessary to prevent becoming trapped in local optimal points. Nevertheless, adding too many populations could lead to longer elapsed time for a single iteration, making it challenging to compute within acceptable time limits. Consequently, the NSGA-II optimization method was not deemed suitable for the simulation conditions in this paper.

Figure 13 displays the deviation changes of each sample at each iteration during calibration using the SMPSO algorithm. SMPSO algorithm's random behavior yields better optimization results for the entire range of cutting conditions than the NSGA-II algorithm. The auto-calibration process terminates after the 23rd iteration, with the optimal solution found during the 14th iteration. The optimal solution indicate deviations of less than 12 % from the experiment. Table 7 presents the sample parameter values with the lowest deviation for the material model.

Figures 14 and 15 show a comparison between the experimentally measured and simulated cutting force and chip thickness. At h_e = 100 and 200 μm, the cutting forces remain relatively constant with cutting speed, while at h_e = 300 μm, the cutting force decreases significantly due to thermal soft-

[2] Intel Xeon Platinum 8468, 48 x 2.1GHz

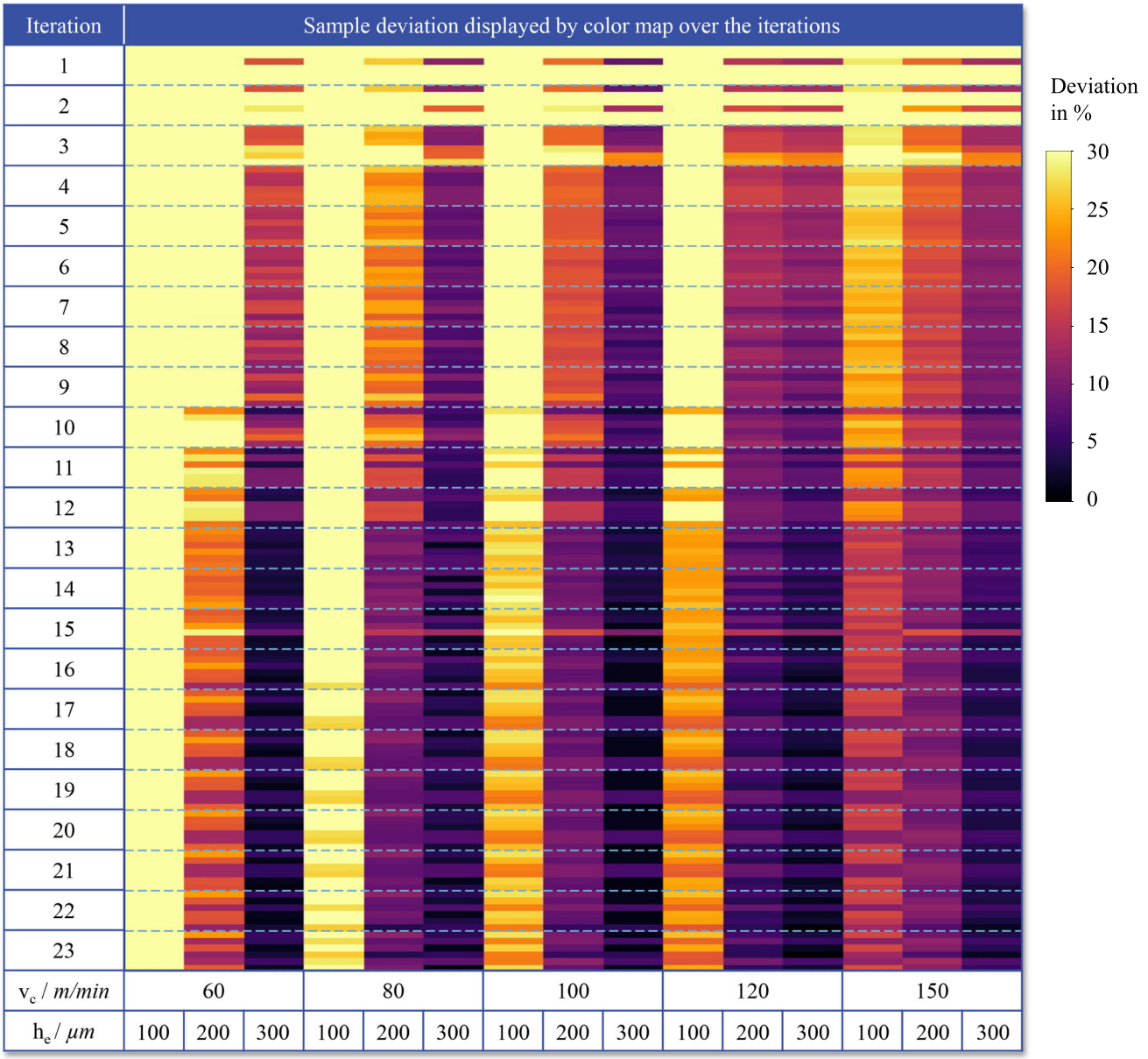

Fig. 12 Deviation values over iterations during automatic calibration for AISI 1045 with NSGA-II

ening of the workpiece material. The simulation results also demonstrate this phenomenon, albeit to a lesser extent. The calibrated material model shows good agreement with the cutting forces, with a deviation within 6 % at $h_e = 200\ \mu m$. However, for $h_e = 100$ and $300\ \mu m$ and low cutting speeds, the deviation is larger, with a maximum of 11 %.

Figure 15 presents the experimental and simulation results of chip thickness. The simulation are in good agreement with the experimental data at $h_e = 200\ \mu m$ but show poor agreement at $h_e = 100$ and $300\ \mu m$. Increasing the cutting speed generally results in a decrease in chip thickness due to temperature-induced thermal softening of the workpiece material and a reduction in friction in the rake face. The reduction in chip thickness leads to a decrease in the chip compression rate, which is defined by the following equation:

$$\lambda_h = \frac{h_{chip}}{h_e} \tag{7}$$

The chip compression rate represents the energy consumed in plastic deformation during metal cutting. When the chip compression rate decreases, the hydrostatic pressure in the loaded material also decreases, which can cause

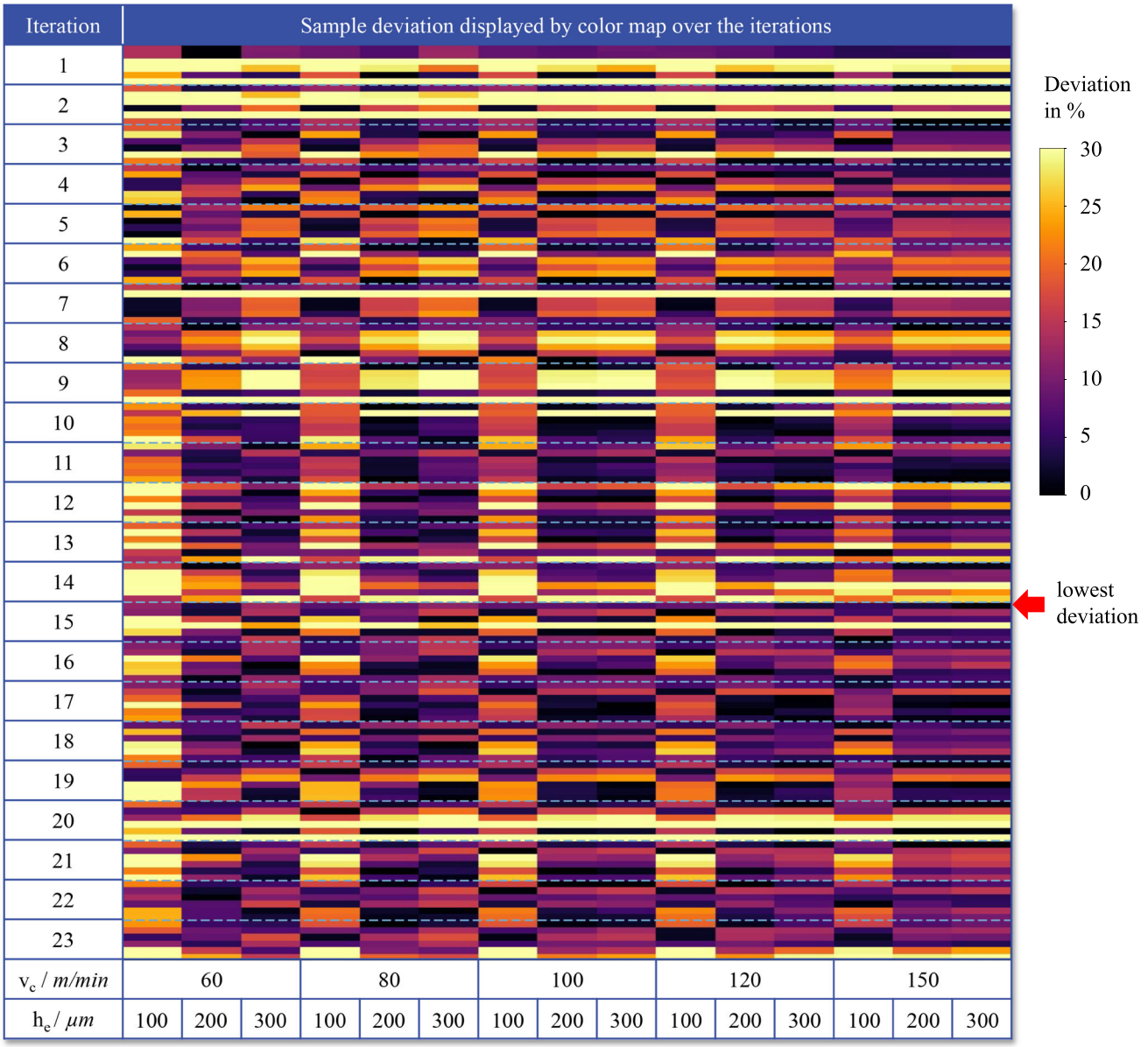

Fig. 13 Deviation values over iterations during automatic calibration for AISI 1045 with SMPSO

strain localization and material damage. Bergs et al. [39] During strain localization, thermal softening dominates over strain hardening, leading to an increase in the local strain rate. Therefore, increasing the cutting speed results in higher strain rates in the primary shear zone.

Chip thickness is affected by various cutting parameters, and to better understand their influence on chip formation, the relationship between chip compression ratio (CCR) and Péclet number (Pe) is plotted in Fig. 16. The Péclet number (Pe) is a dimensionless parameter that compares the con-

Table 7 Calibration results of the material model for AISI 1045

Inverse determined Johnson-Cook material model of AISI 1045							
A [MPa]	B [MPa]	C -	m -	n -	T_m [°C]	T_0 [°C]	$\dot{\varepsilon}_0$ s^{-1}
521.47	456.73	0.037	1.06	0.071	1460	20	1

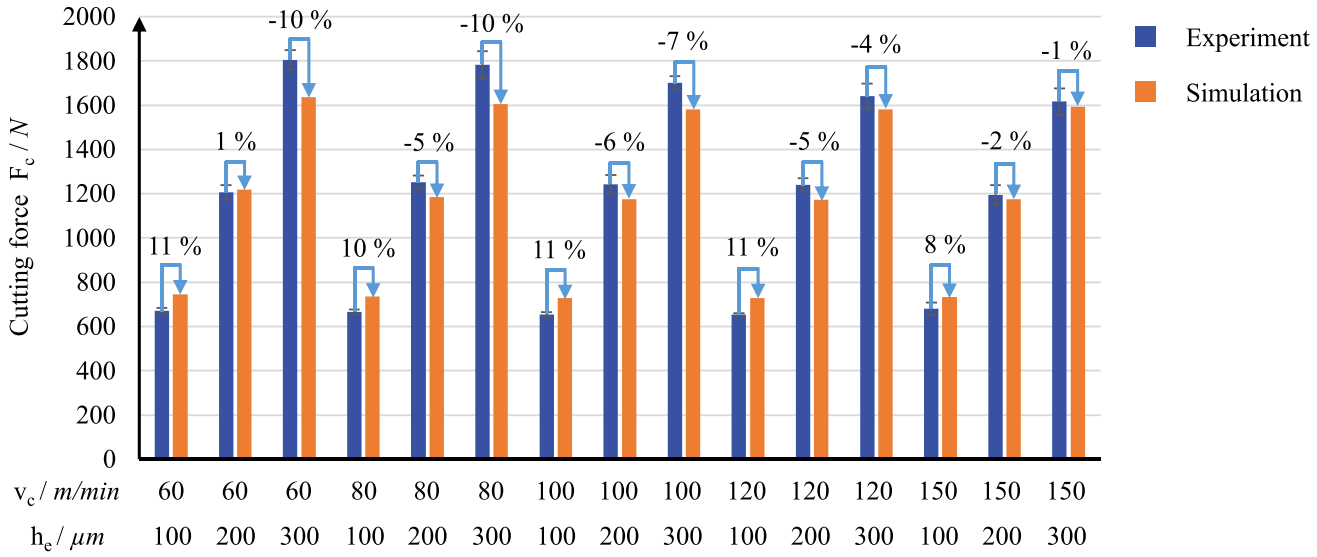

Fig. 14 Comparison of cutting forces between experiment and simulation with the optimal material model for AISI 1045

vection rate to the diffusion rate and can be defined by the following equation:

$$Pe = \frac{v_c \cdot h_e}{\alpha_t} \tag{8}$$

where α_t is the thermal diffusivity of the working material and amounts to $\alpha_t = 13.5 \cdot 10^{-6}\, m^2/s$ for AISI 1045. To enable comparison with previous findings, the data from paper [39] is presented in Fig. 16. The results of this work show a similar trend to those reported in paper [39] and cover a higher Péclet number range. However, the simulations slightly overestimate the chip compression ratio for Péclet numbers smaller than 80. At low Péclet numbers, the heat source propagates faster through the workpiece than the heat wave, resulting in a higher contribution of heat energy to plastic deformation and consequently an increase in the chip compression ratio. Specifically, when the Péclet number is less than 80, the

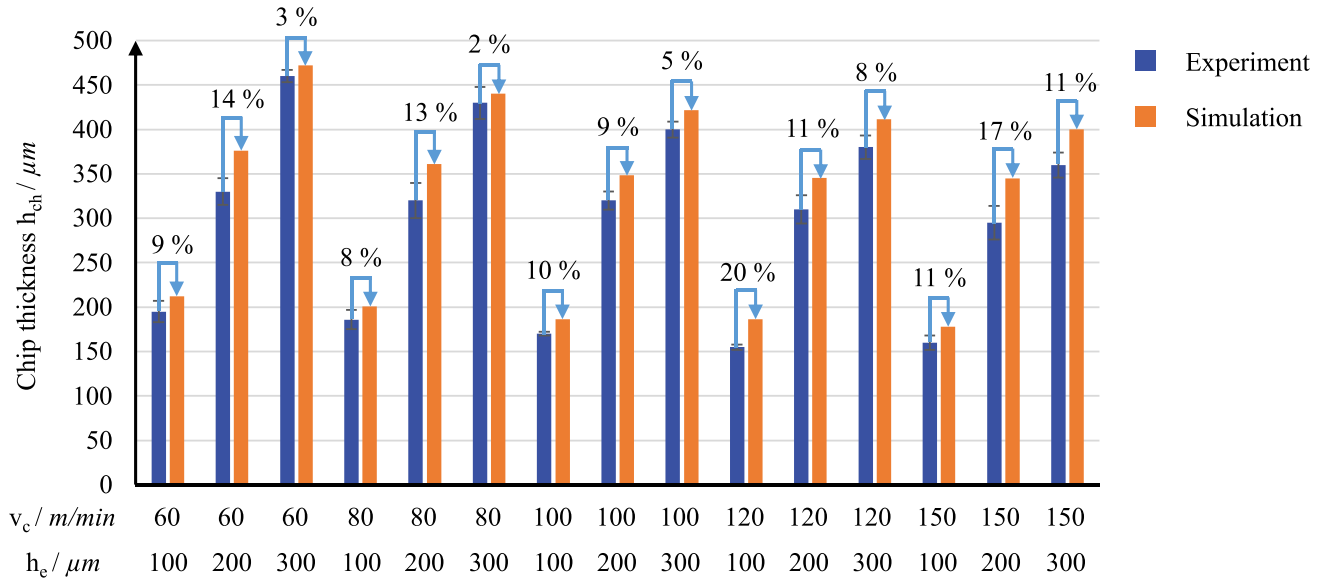

Fig. 15 Comparison of chip thickness between experiment and simulation with the optimal material model for AISI 1045

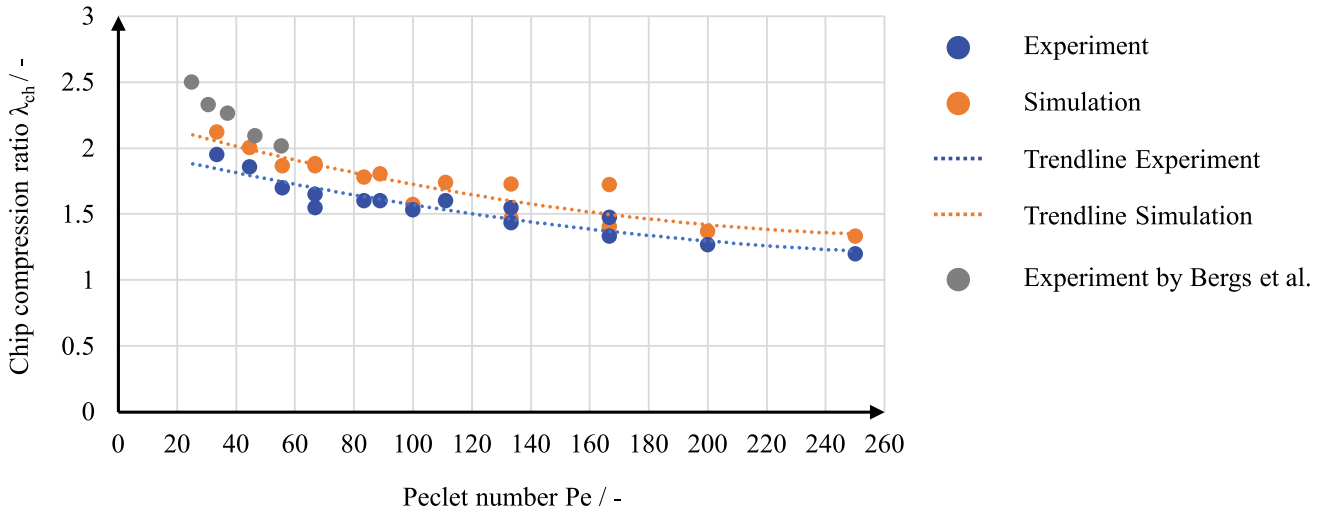

Fig. 16 Dependency of chip compression ratio from the Péclet number when orthogonal cutting AISI 1045

chip compression ratio increases exponentially as the Péclet number decreases.

5.2 Results of X30CrMoN15-1

As the SMPSO algorithm was found to be more effective in calibrating the material model of AISI 1045, it was employed to calibrate the model parameters of X30CrMoN15-1 for finishing conditions. The calibration process relied solely on cutting forces due to the small difference in chip thickness. The deviation values of the simulation results with increasing number of iterations are demonstrated in Appendix.

The deviation values consistently exceed 30 % during the first 6 iterations, but drop significantly starting from the 7 iteration step. Subsequently, the deviation fluctuates randomly throughout the remaining iterations. Despite multiple iterations, the algorithm has failed to find a parameter combination that yields simulation results with deviation values below 11 % up to 30 iterations. Starting from the 31st iteration, the overall parameter results improved.

The optimal material model for X30CrMoN15-1 was achieved after 51 iterations, with the corresponding optimized parameters listed in Table 8. Subsequent iterations did not result in further improvements, and the calibration process was terminated at iteration 60. The SMPSO algorithm's stochastic behavior with the progress of iterations resulted in wider sample movement in the parameter space, facilitating the identification of optimal parameter sets. Therefore, considering limited computational resources, the SMPSO algorithm is a superior choice for calibrating the material model of X30CrMoN15-1.

Figure 17 presents a comparison between the cutting forces obtained from experiments and simulations. The results indicate a significant increase in cutting force with an increase in uncut chip thickness. Although the uncut chip thickness is generally small, the impact of cutting speed on the mechanical temperature load in the cutting area is minimal, resulting in a minor change in cutting force. The simulation results agree well with the experimental data, with deviations of less than or equal to 10 % for all cutting conditions, except for a deviation of 11 % at $v_c = 100\, m/min$ and $h_e = 80\, \mu m$.

6 Conclusion and outlook

Calibration of material models is essential for cutting simulations to ensure an accurate representation of material

Table 8 Calibration results of the material model for X30CrMoN15-1

Inverse determined Johnson-Cook material model of X30CrMoN15-1							
A $[MPa]$	B $[MPa]$	C –	m –	n –	T_m [°C]	T_0 [°C]	$\dot{\varepsilon}_0$ s^{-1}
600	764.24	0.0047	0.94	0.255	1500	25	1

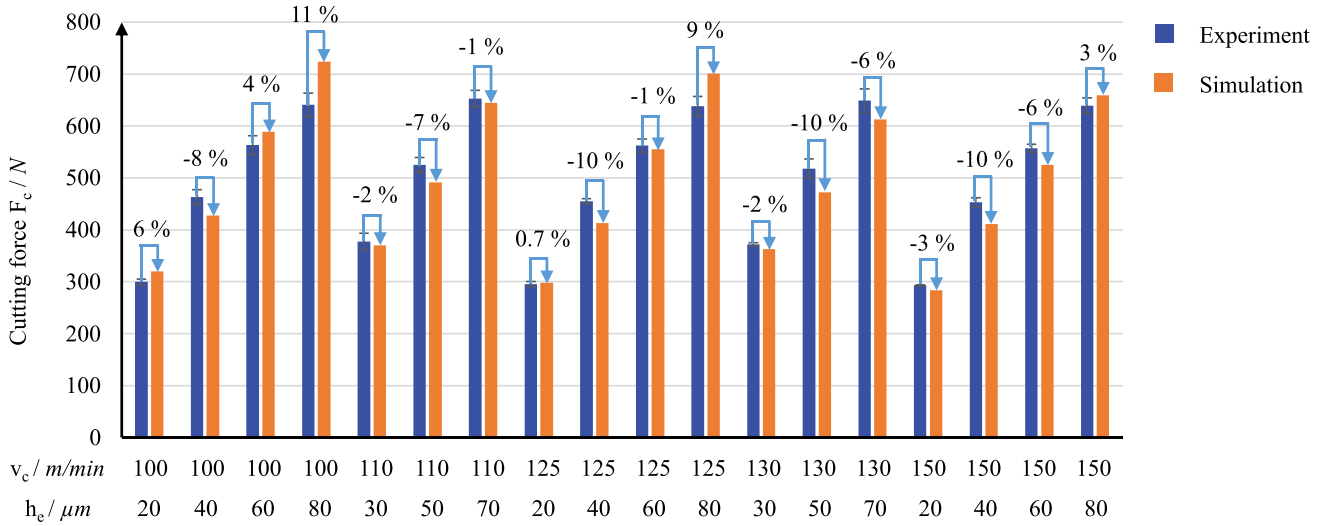

Fig. 17 Comparison of cutting forces between experiment and simulation with the optimal material model for X30CrMoN15-1

behavior under specific cutting conditions. Accurate simulation determines the value of state parameters such as forces, stresses, temperatures and strains. These values are then incorporated into the digital twin of the cutting tools, which captures aspects such as process loads and wear, and into the digital twin of the workpieces, e.g. surface quality and geometric complexity. Bergs et al. [40] This work developed a fully automated procedure that greatly simplifies the calibration of material models. The approach involves an automatic scheme for evaluating simulated chip thickness. Cutting forces and chip thickness are used as the evaluation criteria. To calibrate the material parameters, the performance of the genetic algorithm NSGA-II and the particle swarm algorithm SMPSO are compared with the same number of samples. In addition, the relationship between the chip thickness of AISI1045 and the cutting parameters is analyzed and discussed. The studies lead to the following conclusions:

- Using NSGA-II algorithm for material model calibration, the results demonstrate incremental improvements with each iteration. However, employing SMPSO algorithm results in an initial improvement with increasing iterations, followed by stochastic behavior.
- When using a population size of 6 to calibrate the model, NSGA-II converges to a local optima and fails to identify the global best parameters. On the other hand, SMPSO can discover the global best parameters but its iteration positions are unpredictable.
- SMPSO is a more suitable choice for material model parameter calibration when computational power is limited.
- The experimental and simulated results for AISI 1045 chips indicate that the compression ratio of the chip increases when the Péclet number is low.

Future research should focus on exploring the impact of optimization algorithm parameters, such as population size and mutation factor settings, on model calibration efficiency. It would also be valuable to investigate alternative optimization algorithms for the method proposed in this paper to further improve the calibration process.

Appendix: Deviation over the iterations during calibration of X30CrMoN15-1

This appendix shows the deviations observed during the calibration of the X30CrMoN15-1 material, focusing on the changes that occur at each iteration step. Figures 18 and 19 quantify these deviations and show the values in color. Further background and discussion of these results can be found in Section 5.2 of this paper.

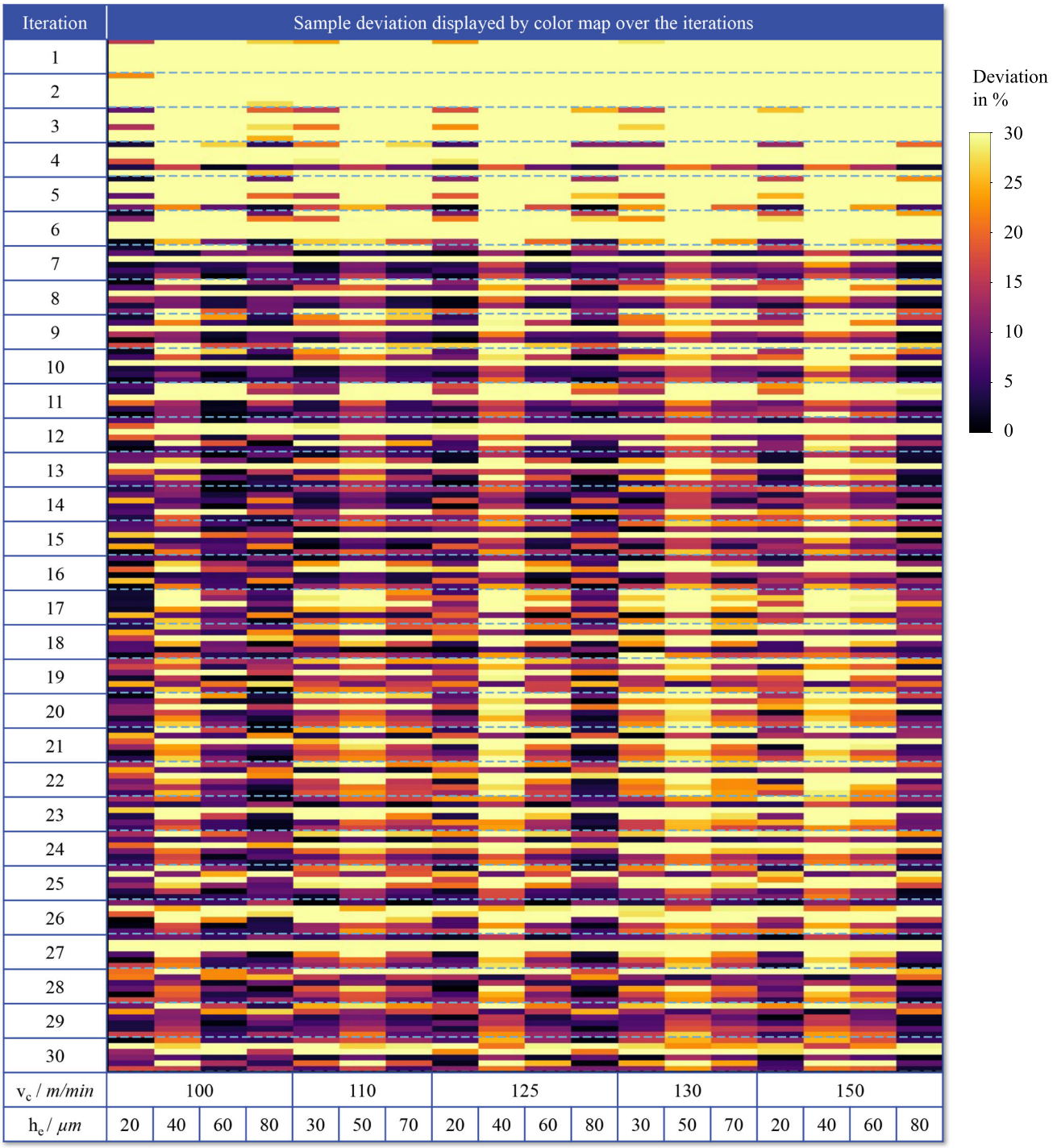

Fig. 18 Deviation values over iterations 1-30 during automatic calibration for X30CrMoN15-1 with SMPSO

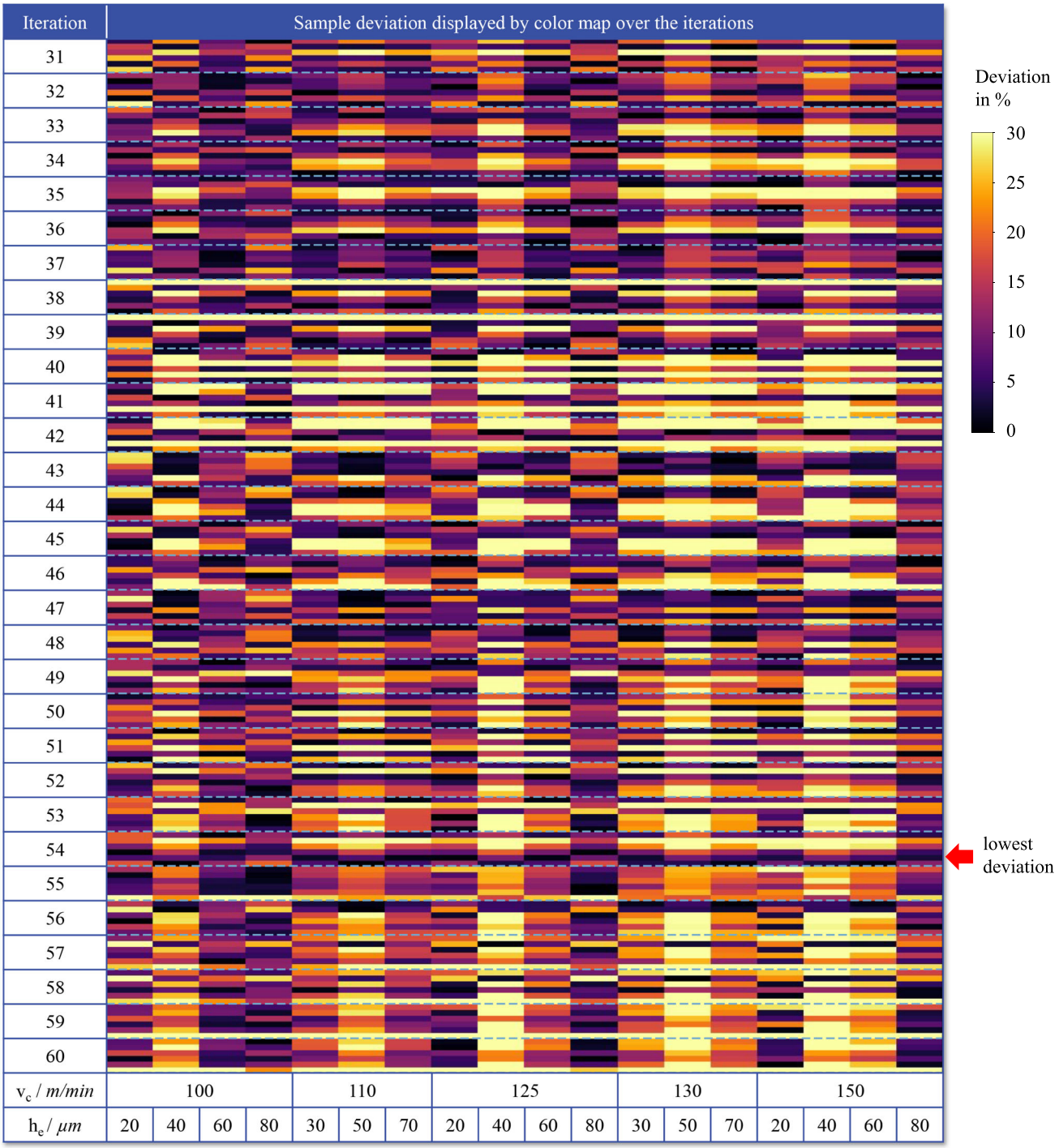

Fig. 19 Deviation values over iterations 31-60 during automatic calibration for X30CrMoN15-1 with SMPSO

Acknowledgements The authors would like to thank the German Research Foundation (DFG) for the funding of the depicted research within the project 426824785. Furthermore, the authors gratefully acknowledge the computing time provided to them at the NHR Center NHR4CES at RWTH Aachen University (project number p0020236). This is funded by the Federal Ministry of Education and Research, and the state governments participating on the basis of the resolutions of the GWK for national high performance computing at universities (www.nhr-verein.de/unsere-partner).

Author Contributions Not applicable

Funding Open Access funding enabled and organized by Projekt DEAL. The research leading to these results received funding from

German Research Foundation (DFG) under Grant Agreement No. 426824785.

Data Availability Not applicable

Code Availability Not applicable

Declarations

Conflicts of interest The authors declare no competing interests.

Ethical Approval Not applicable

Consent to Participate Not applicable

Consent for Publication All participants in the study have read this manuscript and agree to publish the data as well as the contents of the manuscript.

References

1. Grand View Research (2020) Precision engineering machines market size, share & trends analysis report by end-use (automotive, non-automotive), by region (North America, Europe, Asia Pacific, Latin America, Middle East & Africa), and segment forecasts, pp 2021–2028
2. Verband Deutscher Machinen- und Anlagenbau eV (2022) Konjunkturgrafiken zur Jahrespressekonferenz
3. Pau J (ed) (2011) Finite element method in manufacturing processes. ISTE and Wiley, London and Hoboken, NJ
4. Mackerle J (2003) Finite element analysis and simulation of machining: an addendum. Int J Mach Tools Manuf 43(1):103–114. https://doi.org/10.1016/S0890-6955(02)00162-1
5. Klocke F (2018) Fertigungsverfahren 1. Springer, Berlin Heidelberg Berlin, Heidelberg. https://doi.org/10.1007/978-3-662-54207-1
6. Arrazola PJ, Özel T, Umbrello D, Davies M, Jawahir IS (2013) Recent advances in modelling of metal machining processes. CIRP Annals 62(2):695–718. https://doi.org/10.1016/j.cirp.2013.05.006
7. Wang B, Liu Z, Cai Y, Luo X, Ma H, Song Q, Xiong Z (2021) Advancements in material removal mechanism and surface integrity of high speed metal cutting: a review. Int J Mach Tools Manuf 166:103744. https://doi.org/10.1016/j.ijmachtools.2021.103744
8. Melkote SN, Grzesik W, Outeiro J, Rech J, Schulze V, Attia H, Arrazola P-J, M'Saoubi R, Saldana C (2017) Advances in material and friction data for modelling of metal machining. CIRP Annals 66(2):731–754. https://doi.org/10.1016/j.cirp.2017.05.002
9. Kolsky H (1949) An investigation of the mechanical properties of materials at very high rates of loading. Proceedings of the Physical Society. Section B 62(11):676–700. https://doi.org/10.1088/0370-1301/62/11/302
10. Burns TJ, Mates SP, Rhorer RL, Whitenton EP, Basak D (2011) Dynamic properties for modeling and simulation of machining: effect of pearlite to austenite phase transition on flow stress in AISI 1075 steel. Mach Sci Technol 15(1):1–20. https://doi.org/10.1080/10910344.2011.557943
11. Bariani PF, Dal Negro T, Bruschi S (2004) Testing and modelling of material response to deformation in bulk metal forming. CIRP Annals 53(2):573–595. https://doi.org/10.1016/S0007-8506(07)60030-4
12. Özel T, Altan T (2000) Determination of workpiece flow stress and friction at the chip-tool contact for high-speed cutting. Int J Mach Tools Manuf 40(1):133–152. https://doi.org/10.1016/S0890-6955(99)00051-6
13. Shrot A, Bäker M (2012) Determination of Johnson-Cook parameters from machining simulations. Comput Mater Sci 52(1):298–304. https://doi.org/10.1016/j.commatsci.2011.07.035
14. Klocke F, Lung D, Buchkremer S, Jawahir IS (2013) From orthogonal cutting experiments towards easy-to-implement and accurate flow stress data. Mater Manuf Process 28(11):1222–1227. https://doi.org/10.1080/10426914.2013.811738
15. Bäker M (2015) A new method to determine material parameters from machining simulations using inverse identification. Procedia CIRP 31:399–404. https://doi.org/10.1016/j.procir.2015.04.090
16. Chandrasekaran M, Muralidhar M, Krishna CM, Dixit US (2010) Application of soft computing techniques in machining performance prediction and optimization: a literature review. Int J Adv Manuf Technol 46(5–8):445–464. https://doi.org/10.1007/s00170-009-2104-x
17. Yusup N, Zain AM, Hashim SZM (2012) Evolutionary techniques in optimizing machining parameters: review and recent applications (2007–2011). Expert Syst Appl 39(10):9909–9927. https://doi.org/10.1016/j.eswa.2012.02.109
18. Özel T, Karpat Y (2007) Identification of constitutive material model parameters for high-strain rate metal cutting conditions using evolutionary computational algorithms. Mater Manuf Process 22(5):659–667. https://doi.org/10.1080/10426910701323631
19. Hardt M, Jayaramaiah D, Bergs T (2021) On the application of the particle swarm optimization to the inverse determination of material model parameters for cutting simulations. Modelling 2(1):129–148. https://doi.org/10.3390/modelling2010007
20. Özel T, Zeren E (2006) A methodology to determine work material flow stress and tool-chip interfacial friction properties by using analysis of machining. J Manuf Sci Eng 128(1):119–129. https://doi.org/10.1115/1.2118767
21. Puls H, Klocke F, Lung D (2014) Experimental investigation on friction under metal cutting conditions. Wear 310(1–2):63–71. https://doi.org/10.1016/j.wear.2013.12.020
22. Kibireva A, Meurer M, Schraknepper D, Bergs T (2023) Experimental and simulative investigation of thermomechanical loads in the cutting zone by machining X30CrMoN-15-1 steel with CBN tools. Procedia CIRP 118:489–494. https://doi.org/10.1016/j.procir.2023.06.084
23. Gao Y, Ko JH, Lee HP (2018) 3D coupled Eulerian-Lagrangian finite element analysis of end milling. Int J Adv Manuf Technol 98(1–4):849–857. https://doi.org/10.1007/s00170-018-2284-3
24. Liu H, Helmig T, Gerhard N, Kneer R, Bergs T (2023) Numerical and experimental determination of contact heat transfer during orthogonal cutting. Procedia CIRP 117:329–334. https://doi.org/10.1016/j.procir.2023.03.056
25. Benson DJ (1992) Computational methods in Lagrangian and Eulerian hydrocodes. Comput Methods Appl Mech Eng 99(2–3):235–394. https://doi.org/10.1016/0045-7825(92)90042-I

26. Johnson GR, Cook WH (1985) Fracture characteristics of three metals subjected to various strains, strain rates, temperatures and pressures. Eng Fract Mech 21(1):31–48. https://doi.org/10.1016/0013-7944(85)90052-9
27. Jaspers SPFC, Dautzenberg JH (2002) Material behaviour in conditions similar to metal cutting: flow stress in the primary shear zone. J Mater Process Technol 122(2–3):322–330. https://doi.org/10.1016/S0924-0136(01)01228-6
28. Ee KC, Dillon OW, Jawahir IS (2005) Finite element modeling of residual stresses in machining induced by cutting using a tool with finite edge radius. Int J Mech Sci 47(10):1611–1628. https://doi.org/10.1016/j.ijmecsci.2005.06.001
29. Zouhar J, Piska M (2008) Modelling the orthogonal machining process using cutting tools with different geometry. MM Sci J 2008(03): 49–52. https://doi.org/10.17973/MMSJ.2008
30. Saez-de-Buruaga M, Esnaola JA, Aristimuno P, Soler D, Björk T, Arrazola PJ (2017) A coupled Eulerian Lagrangian model to predict fundamental process variables and wear rate on ferrite-pearlite steels. Procedia CIRP 58:251–256. https://doi.org/10.1016/j.procir.2017.03.194
31. Treppmann C (2001) Fließverhalten Metallischer Werkstoffe Bei Hochgeschwindigkeitsbeanspruchung: Aachen. Techn Hochsch, Diss, p 2001
32. Klocke F, Lung D, Buchkremer S (2013) Inverse identification of the constitutive equation of Inconel 718 and AISI 1045 from FE machining simulations. Procedia CIRP 8:212–217. https://doi.org/10.1016/j.procir.2013.06.091
33. He T, Wang H, Yoon SW (2018) Comparison of four population-based meta-heuristic algorithms on pick-and-place optimization. Procedia Manuf 17:944–951. https://doi.org/10.1016/j.promfg.2018.10.112
34. Omidvar MN, Li X, Yao X (2022) A review of population-based metaheuristics for large-scale black-box global optimization–part i. IEEE Trans Evol Comput 26(5):802–822. https://doi.org/10.1109/TEVC.2021.3130838
35. Vikhar PA (2016) Evolutionary algorithms: a critical review and its future prospects. 2016 International conference on global trends in signal processing, information computing and communication (ICGTSPICC), 261–265. https://doi.org/10.1109/ICGTSPICC.2016.7955308
36. Deb K, Pratap A, Agarwal S, Meyarivan T (2002) A fast and elitist multiobjective genetic algorithm: NSGA-II. IEEE Trans Evol Comput 6(2):182–197. https://doi.org/10.1109/4235.996017
37. Kennedy J, Eberhart R (1995) Particle swarm optimization. Proceedings of ICNN'95 - international conference on neural networks, pp 1942–1948. https://doi.org/10.1109/ICNN.1995.488968
38. Nebro AJ, Durillo JJ, Garcia-Nieto J, Coello Coello CA, Luna F, Alba E (2009) SMPSO: a new PSO-based metaheuristic for multi-objective optimization. 2009 IEEE Symposium on computational intelligence in multi-criteria decision-making(MCDM), pp 66–73. https://doi.org/10.1109/MCDM.2009.4938830
39. Bergs T, Abouridouane M, Meurer M, Peng B (2021) Digital image correlation analysis and modelling of the strain rate in metal cutting. CIRP Annals 70(1):45–48. https://doi.org/10.1016/j.cirp.2021.04.055
40. Bergs T, Biermann D, Erkorkmaz K, M'Saoubi R (2023) Digital twins for cutting processes. CIRP Annals. https://doi.org/10.1016/j.cirp.2023.05.006